Available online at www.sciencedirect.com

ScienceDirect

International Journal of Solids and Structures 45 (2008) 4098–4113

INTERNATIONAL JOURNAL OF SOLIDS AND STRUCTURES

www.elsevier.com/locate/ijsolstr

Micromechanical modeling of the microbond test to quantify the interfacial properties of fiber-reinforced composites

M. Nishikawa [a], T. Okabe [b,*], K. Hemmi [a], N. Takeda [c]

[a] *Department of Aeronautics and Astronautics, The University of Tokyo, c/o Transdisciplinary Sciences Building, Mailing Box 311, 5-1-5 Kashiwanoha, Kashiwa-shi, Chiba 277-8561, Japan*

[b] *Department of Aerospace Engineering, Tohoku University, 6-6-01 Aoba-yama, Aoba-ku, Sendai 980-8579, Japan*

[c] *Department of Advanced Energy, Graduate School of Frontier Sciences, The University of Tokyo, c/o Transdisciplinary Sciences Building, Mailing Box 302, 5-1-5 Kashiwanoha, Kashiwa-shi, Chiba 277-8561, Japan*

Received 31 October 2007; received in revised form 25 January 2008

Available online 6 March 2008

Abstract

The present study has focused on achieving a micromechanical understanding of the microbond test, which involves pulling a fiber out of a bead of matrix (i.e. droplet) through a knife-edge, in order to quantify the interfacial fracture properties of fiber-reinforced composites. According to the microbond test results for carbon-fiber and epoxy-resin system, matrix cracking occurred during the fiber pullout, in addition to the debonding at the fiber–matrix interface. Therefore, in evaluating the fracture properties of the fiber–matrix interface, we should pay attention to the coupling effects of matrix failure and interfacial debonding on the test results. Then, we discuss how to best extract the interfacial properties while excluding the influence of matrix plasticity and cracking, using numerical simulations. The key mechanism demonstrated here is that the pullout force, in the cases where the influence of matrix cracking is negligible, appears as the upper limit among the experimental data of the pullout force for a constant initial embedded length of the fiber in the matrix. For this reason, the upper-limit data all over the range of embedded fiber length in experiments can be reasonably evaluated by the simulation focusing on the debonding process with matrix plasticity. This evaluation technique is effective as a way of extracting interfacial properties appropriately from microbond test results.

Keywords: Fiber-reinforced composites; Microbond test; Interface; Matrix cracking; Micromechanical modeling

1. Introduction

Carbon fiber-reinforced plastics (CFRPs) are currently being investigated for use as general industrial materials, such as in automobile applications, in response to the recent development of lighter aircraft structures. In these applications, efforts to improve the mass production techniques employed are increasingly required in order to obtain the desired material strength at low cost. The desired material strength is not

* Corresponding author. Tel.: +81 22 795 6984; fax: +81 22 795 6983.
E-mail address: okabe@plum.mech.tohoku.ac.jp (T. Okabe).

0020-7683/$ - see front matter © 2008 Elsevier Ltd. All rights reserved.
doi:10.1016/j.ijsolstr.2008.02.021

an easy target for fiber-reinforced composites because the strength and toughness of these composites depend on the properties (i.e. the strength and toughness) of the fiber/matrix interface. Thus, a method for quantifying the interfacial properties must be established to support the design of fiber-reinforced composites. However, how to evaluate these basic interfacial properties remains a controversial issue among researchers of composite materials.

Test methods using single-fiber model composites, such as pullout, microbond, and pushout tests, are helpful in extracting the debonding process of the interface from the overall damage process of a composite. In particular, the microbond test (Miller et al., 1987) is a simple fiber pullout technique for evaluating shear failure of the fiber–matrix interface. The microbond test involves pulling a fiber out of a bead of matrix (i.e. droplet) through a knife-edge (as shown in Fig. 1), accompanied by the debonding at the fiber–matrix interface, and then it evaluates the interfacial fracture properties based on the resulting force required in the pullout. This technique is quite useful for small-diameter fibers, such as carbon fibers, because the fiber pullout can be completed without fiber breakage. However, it has frequently been pointed out that the microbond test fails to quantify the "true" interfacial properties representing the interfacial fracture, partly because the interfacial properties obtained from the microbond test using conventional data-reduction techniques (e.g. the averaged interfacial shear strength (IFSS)) are not consistent with those determined using other test methods (Herrera-Franco and Drzal, 1992). In addition, many researchers (such as Zinck et al. (2001)) have reported significant data scatter as a limiting aspect of the microbond test. This inconvenience is caused by the fact that the micromechanical modeling for the microbond test has not been well developed and the overall damage process during the test is not well understood. This issue must be solved by the contributions of a detailed numerical analysis.

Recent researches (Bi et al., 2002; Tsai et al., 2005) have contributed to finite-element (FE) modeling of the fiber pullout and pushout tests. These models address the interfacial fracture during the tests, utilizing interface elements embedding the damage process zone onto the fiber–matrix interface. This framework had been frequently applied to the fracture at the fiber–matrix interface in composites, first in Nutt and Needleman (1987), and then extended in Tvergaard (1990), etc. In most interface elements, the model of the damage process zone was constructed based on the conventional fracture mechanics. (This type of model was referred to as an embedded process zone (EPZ) model in Hutchinson and Evans, 2000.) Overall, these approaches to interfacial fracture are also effective for the modeling of single-fiber test methods. Additionally, the predicted results of the debonding process during the tests can be utilized to obtain interfacial fracture properties (strength and toughness) of the composites through their fitting to the experimental data.

In applying these approaches to the modeling of microbond tests for small-diameter fibers, however, some difficulties arise. In microbond tests, actual experiments reveal that part of each droplet remains on the fiber after it is pulled out of the matrix (Zinck et al., 2001), and thus the fiber pullout cannot be characterized by the debonding all over the interface (i.e. pure debonding process). The coupling effects of matrix failure and debonding process on the test results should be discussed in order to reasonably extract the interfacial fracture properties based on the microbond test. This point has not been discussed in the micromechanical modeling and analysis of the microbond test.

For this purpose, the present study has focused on achieving a micromechanical understanding of the microbond test, with consideration given to matrix failure, in order to quantify the interface properties of fiber-reinforced composites. The present approach to interfacial fracture is based on the EPZ model. First,

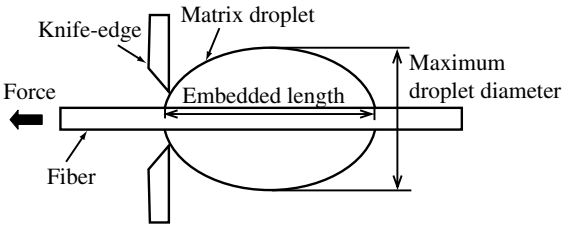

Fig. 1. Schematic of the microbond test configuration.

we conducted microbond tests using T800S carbon-fiber specimens with epoxy-resin droplets. The experimental setup and results are presented in Section 2. The experimental results and FE modeling reinforces our understanding that the inherent difficulty in controlling the knife-edge position causes the variation of matrix cracking, and consequently the data scatter in the microbond tests. We then discuss how to best extract the interfacial properties while excluding the influence of matrix plasticity and cracking in Section 3. Here, our basic idea for evaluating experimental results is that the upper limit of the pullout force, among the experimental data for a constant initial embedded length of the fiber in the matrix, is controlled almost entirely by a pure debonding process. This basic mechanism is finally verified in Section 4, using numerical simulations to discuss the influence of matrix cracking on the pullout process in the microbond test. These discussions contribute to the appropriate evaluation of interfacial fracture based on the microbond test results.

2. Microbond test

2.1. Experiment

We conducted microbond tests using T800S carbon fiber with 5 μm fiber diameter, provided by Toray Industries, and epoxy resin (Bisphenol-A type epoxy resin (Epikote 828) with triethylenetetramine (TETA) as curing agent in a 100/11 ratio). The specimen consisted of a fiber embedded in matrix droplets. A steady displacement was applied to the free end of the fiber to pull it out of the matrix through a knife-edge, as illustrated in Fig. 1. The machine used in the test was developed in our previous study (Zhao et al., 1996). The test was conducted at room temperature, with the rate of fiber-end displacement set to 0.10 mm/min. The fiber pullout was conducted under observation with an optical microscope. During the test, the force applied to the free-fiber end was measured with a sensitive load cell of 5 N. Here it should be noted that our experimental setup could not control the exact knife-edge position from the fiber, and thus the variation in the knife-edge position from one test to another was inherently included in the experimental data. It will be clarified in the following sections that this difficulty in controlling the knife-edge position causes the variation of the size and position of matrix cracking, which influences the pullout process.

Fig. 2(a) presents a typical force history obtained by the experiment. The fiber-end force increases almost proportionally to the applied displacement until it reaches a maximum force and then drops. The pullout force F_d, measured as the maximum force applied to the fiber end, is then plotted as a function of the embedded length l of the fiber in the droplet in Fig. 2(b). The lines evaluated by the interfacial shear strength (IFSS) criterion and by the analytical model based on the energy-based criterion (Scheer and Nairn, 1995) are also included in the figure.

$$F_d = 2\pi r_f l \cdot \tau_{cr} \quad \text{(IFSS)} \tag{1}$$

$$F_d = F_d(l, G_c, \Delta T) \quad \text{(Energy-based criterion)} \tag{2}$$

Here, τ_{cr} is the interfacial shear strength, G_c is the critical energy release rate, r_f is the fiber radius, and ΔT is the temperature change from the stress-free temperature (−80 K). The experimental results have a large scatter in the pullout force, and the interfacial parameters estimated by fitting with the experimental data vary excessively. IFSS varies from 64 to 108 MPa (average: 92.3 MPa), and G_c varies from 81 to 205 J/m^2 (average: 131.5 J/m^2).

This issue is inherent for small-diameter fibers in attempts to obtain a quantitative fit with experiments. Here, the typical fiber breaking strain is about 2.0% according to the data sheet of the supplier. Therefore, when fiber pullout can be completed without fiber breakage, the pullout force is at most 0.12 N for the present material system, according to the fiber breaking strain and Hooke's law. Then the fiber embedded length where pullout data is available is at most 75 μm, as seen in Fig. 2. In contrast, in the previous literature where existing theoretical models have worked well (e.g. Scheer and Nairn, 1995), the target material system provides a wide range of embedded lengths in the experiments. For example, Scheer and Nairn (1995) demonstrate a quantitative fit with experiments for pulling E-glass fibers (21 μm diameter) out of epoxy droplets, where the maximum embedded length is about 0.45 mm. In their case, the interfacial property may be determined by use of a least-squares regression, because of the wide range of available experimental data.

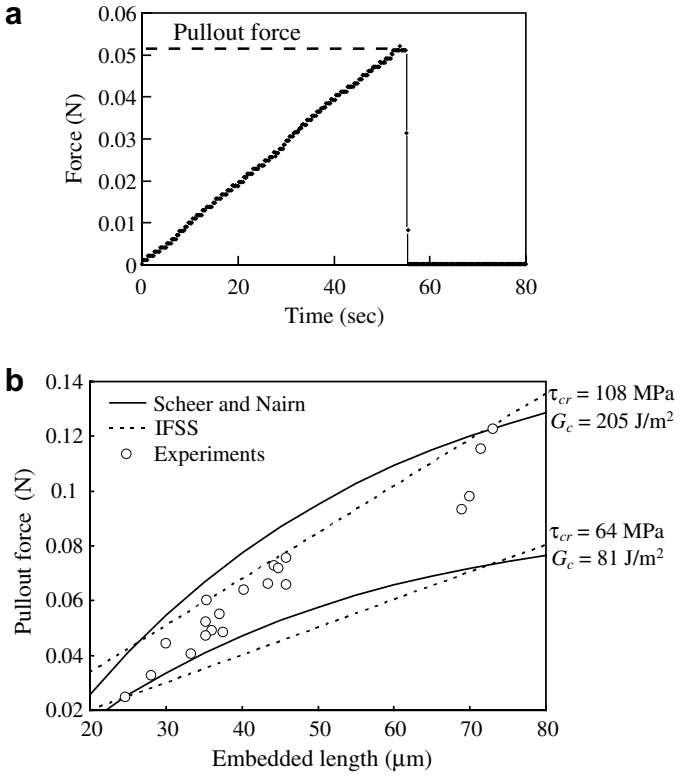

Fig. 2. Microbond tests for T800S carbon-fiber and epoxy-resin system. (a) Typical fiber-end force history during the fiber pullout. (b) Pullout force as a function of the embedded length.

Fig. 3 presents photographs of a droplet remaining on a fiber after the pullout, observed with a scanning electron microscope (SEM). Matrix cracking from the knife-edge position (Fig. 3(a)) and in the meniscus region (Fig. 3(b)) can be seen in the figure. This fact shows that the fiber was not pulled out under a pure debonding process in the microbond tests. (Pure debonding process means that the fiber pullout was completed by the debonding all over the interface.) In the case of Fig. 3(b), the size of the matrix cracking is small, and thus we can consider that the fiber was pulled out almost under a pure debonding process. In fact, it will be shown in Section 4 that the influence of the matrix cracking in the meniscus region on the pullout force was negligible. In contrast, the size of the matrix cracking seen in Fig. 3(a) is not negligible compared with the fiber embedded length. The influence of this matrix cracking on the test results, however, has not been considered in the previous works because the fracture phenomenon during the pullout in experiments is usually not discernible under an optical microscope. This is a major issue in applying conventional evaluation techniques to the experimental results. The influence of matrix cracking in the droplet must be considered in order to extract interfacial fracture from microbond test results.

2.2. Matrix cracking depending on the knife-edge position

To examine the underlying mechanism of the matrix cracking process as seen in microbond tests, we conducted crack path predictions using numerical simulations. We demonstrate the effect of the knife-edge position, which is difficult to control in the experiments, on the matrix cracking process.

Fig. 4 depicts the axisymmetric finite-element model used in the simulation. The actual profile of a matrix droplet was considered using Carroll's theory (Carroll, 1976; Ash et al., 2003). According to the procedure described in Appendix A, the profile of a matrix droplet can be determined as a function of the contact angle of the droplet with the fiber. To determine the profile based on experiments, we first measured the relationship

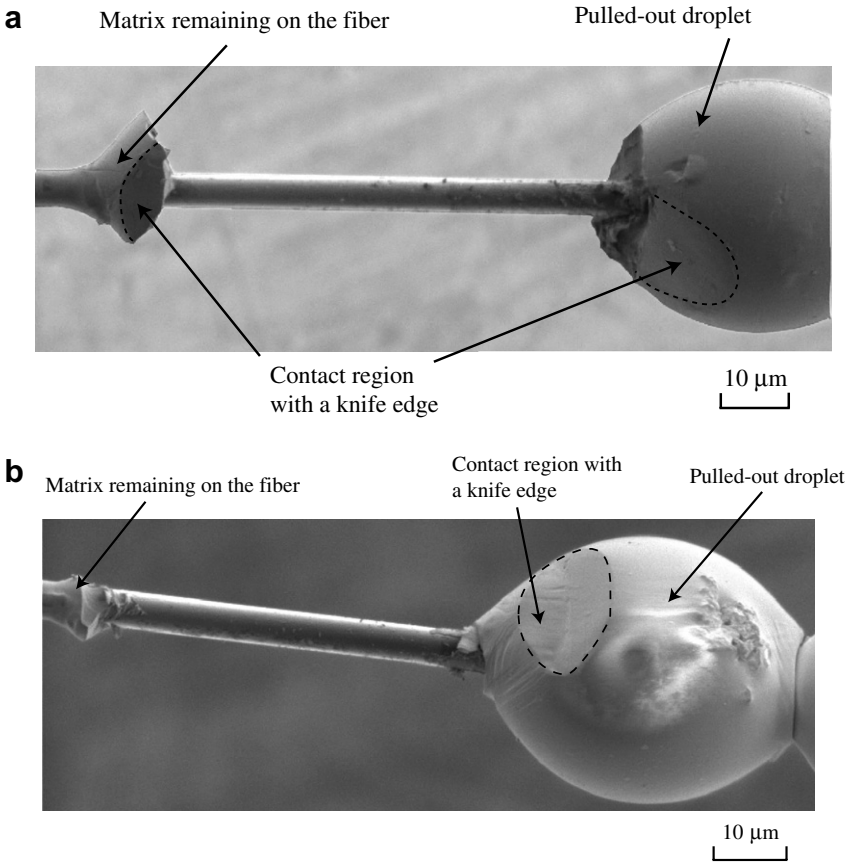

Fig. 3. SEM observations of a droplet remaining on the fiber after pullout. (a) When the knife-edge position is near the fiber. (b) When the knife-edge position is far from the fiber.

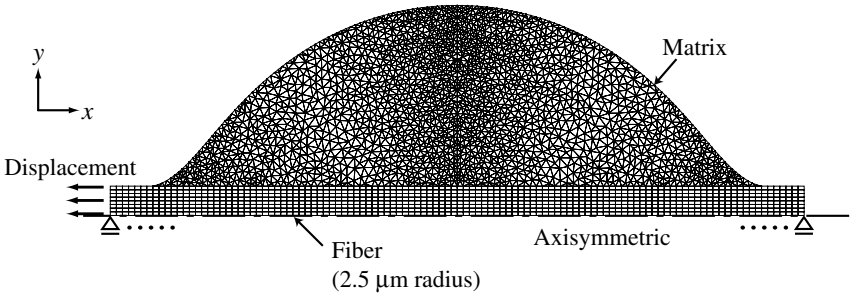

Fig. 4. Finite-element model for the single-fiber and matrix-droplet system.

between the embedded length of the fiber in the droplet and the maximum droplet diameter, using SEM photographs of arbitrary droplets on a fiber prepared with the same procedure as that used for the microbond specimens. Fig. 5 plots the measured relationship between the fiber embedded length and the maximum droplet diameter. We then determined that the theoretical line using the contact angle $\theta = 12.0°$ reproduced the measured relationship in Fig. 5. We also confirmed that we can reproduce the profile of the matrix droplet by substituting the obtained contact angle into the theory, as demonstrated in Fig. 6. In the following, we present the results when the embedded length of the fiber in the model was set to 52 μm as a typical example (Fig. 4).

In the finite-element model, fiber was represented as an elastic orthotropic material, consisting of nine-node isoparametric quadrilateral elements, and the matrix was represented by a J_2 flow elastic–plastic material, con-

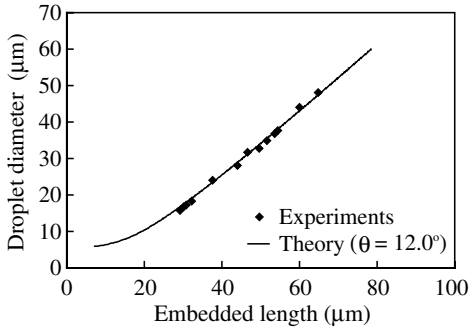

Fig. 5. Relationship between embedded fiber length and droplet maximum radius to determine the droplet profile. The theoretical line in the figure is based on Carroll (1976).

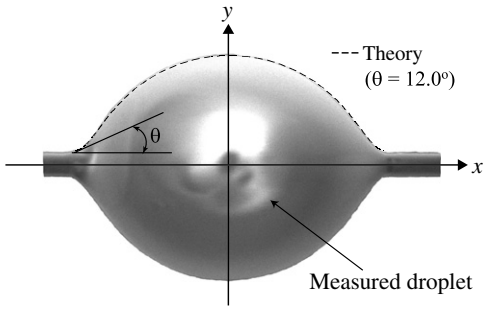

Fig. 6. Comparison of the profile of a matrix droplet between experiment and theory.

sisting of six-node triangle elements. The constitution law of the matrix was introduced through the bi-linear stress–strain relation, assuming a linear-isotropic hardening function. The material properties are listed in Table 1. The matrix plastic properties in Table 1 were obtained by tensile tests. All the simulations in this paper included the effect of the thermal residual stress generated during the cooling process in the specimen fabrication.

Finally, the matrix cracking was addressed, utilizing one-parameter damage mechanics model for the cracking in epoxy-matrix (Nishikawa et al., in preparation) This procedure is described in Appendix B. The aim of this section is to understand the experimental phenomena in microbond tests qualitatively, and thus the detailed discussion about the employed matrix cracking model is left to our future discussion.

Table 1
Material properties used in the simulation

Fiber axial modulus	294 GPa
Fiber transverse modulus	14 GPa
Fiber axial Poisson's ratio	0.2
Fiber transverse Poisson's ratio	0.35
Fiber axial shear modulus	18 GPa
Fiber transverse shear modulus	14 GPa
Fiber axial thermal expansion coefficient	-0.4×10^{-6} (/K)
Fiber transverse thermal expansion coefficient	3×10^{-5} (/K)
Fiber diameter	5 μm
Matrix modulus	3.5 GPa
Matrix Poisson's ratio	0.31
Matrix yield stress	73 MPa
Matrix plastic tangent modulus	75 MPa
Matrix thermal expansion coefficient	4×10^{-5} (/K)

With this model, we present the matrix cracking process during fiber pullout in a microbond test. The simulation was conducted by controlling the fiber-end displacement. The simulation was based on a static, nonlinear incremental analysis. In addition, the boundary conditions given by the knife-edge were reproduced by fixing the corresponding nodes of the droplet boundary whenever they reached the knife-edge as a consequence of deformation.

We present the simulated results analyzed with two cases of boundary conditions: (a) with the knife-edge near the fiber (5.0 mm away from the interface) and (b) with the knife-edge far from the fiber (11.5 mm away from the interface). Fig. 7 depicts the simulated results of the matrix cracking process as the applied force increases for two cases of the knife-edge position. When the knife-edge position is near the fiber (Fig. 7(a)), the fiber-end force and the contact force exerted by the knife-edge, which act in opposite directions, contribute to the cracking from the knife-edge position. The matrix cracking then propagates until it reaches the inter-

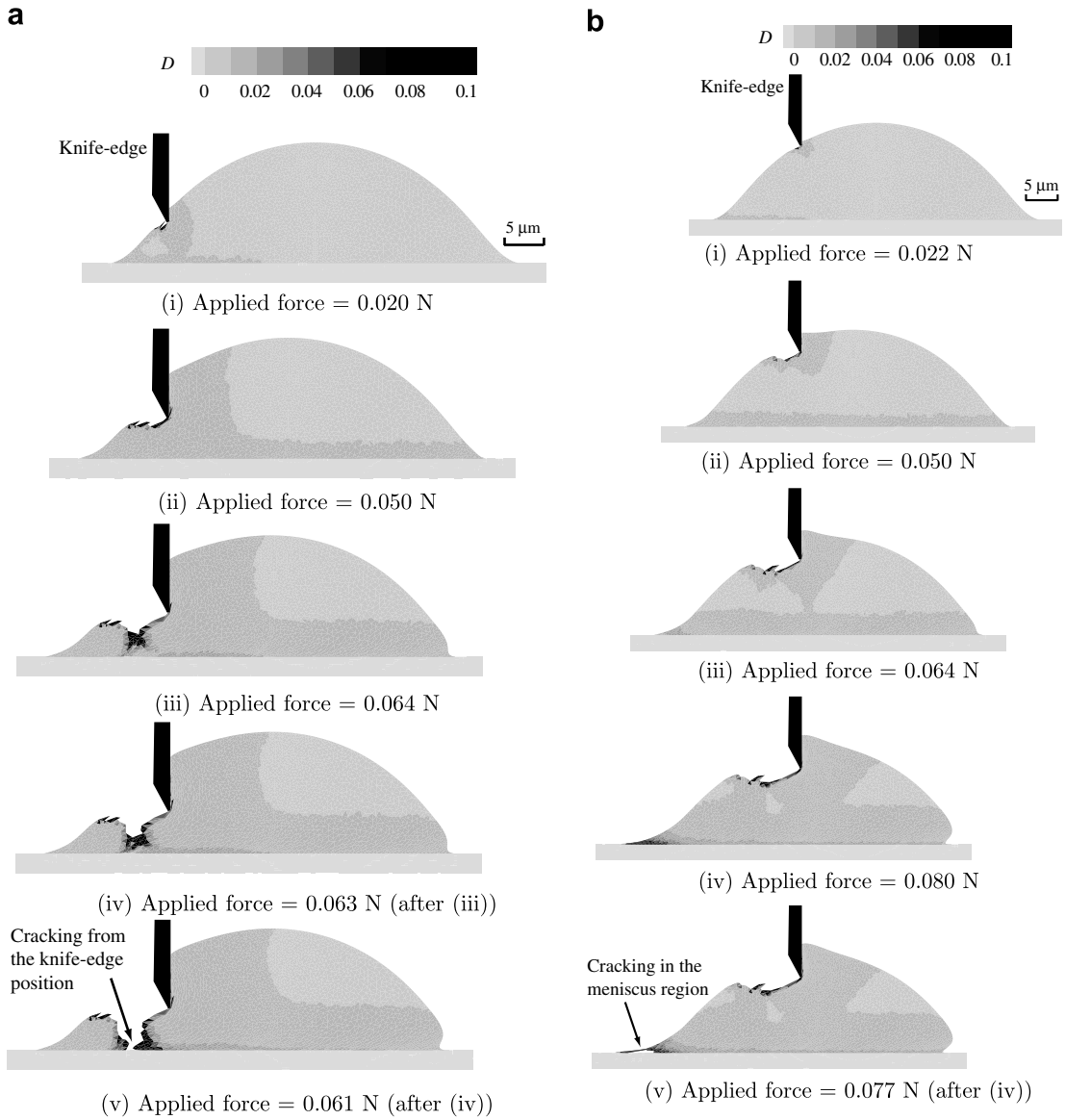

Fig. 7. Simulated results of the matrix cracking process as the applied force increases when the knife-edge position is varied. (a) When the knife-edge position is near the fiber. (b) When the knife-edge position is far from the fiber.

face. In contrast, when the knife-edge position is far from the fiber (Fig. 7(b)), the matrix crack emanating from the knife-edge position does not grow to the interface, and increasing the applied force causes cracking in the meniscus region (Fig. 7(b)-(v)). Fig. 8 plots the distributions of von-Mises effective stress in a droplet for two cases of knife-edge position. The stress concentration in the droplet changes as the knife-edge position is varied, as demonstrated by comparing Fig. 8(a) and (b). This difference of stress concentration leads to variations in the cracking position depending on the knife-edge position. In addition, this tendency of crack paths depending on the knife-edge position as seen in these figures is consistent with the experimental results in Fig. 3.

From these results, we can conclude that the knife-edge position determines the position of matrix cracking. In particular, when the knife-edge position is near the fiber, the matrix cracking initiated from the knife-edge position reaches the interface, and the significantly large matrix cracking occurs. Therefore, according to the knife-edge position, the large matrix cracking occurs in some tests, and then the results obtained from these tests do not evaluate a pure interfacial fracture process. These facts imply that the inability to control the exact knife-edge position causes difficulties to evaluate interfacial properties based on the microbond test. In our simulation, if the knife-edge position is kept more than approximately twice the fiber diameter away from the interface, the fiber can be pulled out without causing a significant matrix cracking, as illustrated in Fig. 7(b). This is an ideal condition of microbond tests in order to evaluate the appropriate interface properties.

However, the precise control of the knife-edge position in microbond tests is generally difficult. Considering the realistic situation, it is rather desirable to extract the interfacial properties from microbond tests while excluding the influence of matrix failure, instead of controlling the knife-edge position. This will be discussed in Sections 3 and 4.

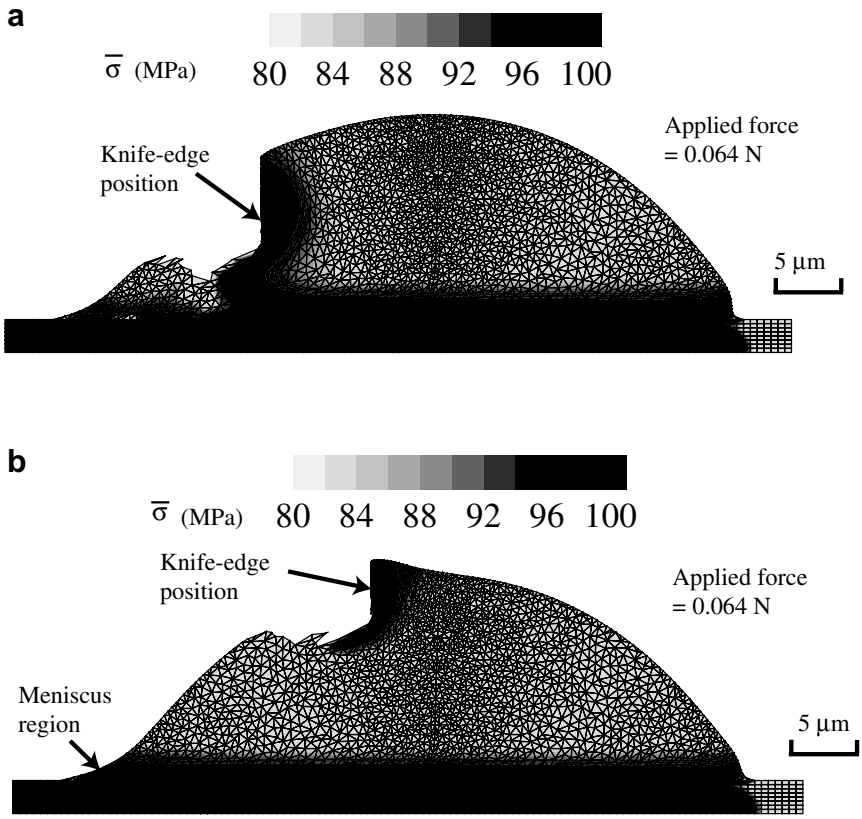

Fig. 8. Comparison of the simulated stress distribution when the knife-edge position is varied. (a) When the knife-edge position is near the fiber. (b) When the knife-edge position is far from the fiber.

3. Estimation of the interfacial properties from microbond tests

In this section, we discuss how to best extract the interfacial properties while excluding the influence of matrix plasticity and cracking. At the beginning of this section, we summarize our idea for evaluating the experimental results. The experimental observations in Fig. 3 reveal the occurrence of matrix cracking during the pullout process. When matrix cracking occurs, it can be supposed that the residual length of the fiber embedded in the droplets decreases due to the matrix cracking. The pullout force then decreases due to the reduced embedded length. We note here that the experimental results reveal cases where matrix cracking occurs in the meniscus region and is very small, as seen in Fig. 3(b). In this case, we can say that the residual embedded length of the fiber is almost the same as the initial embedded length and thus that the pullout force is controlled almost entirely by the pure debonding process. Therefore, the pure debonding case will be the case that gives the maximum residual length of the fiber, and thus the maximum pullout force, among the experimental data for a constant initial embedded length. Based on this idea, we evaluate the interfacial properties based on the upper limit of the experimental results by simulating debonding growth.

For this purpose, we utilized numerical simulations for the interfacial debonding process during the fiber pullout in a microbond test. The present simulation is based on the EPZ model for interfacial fracture.

3.1. Numerical model

Fig. 9 illustrates a typical axisymmetric model used in the simulation. To compare the results with that of the conventional evaluation method presented in Section 2.1, we used a simple two-cylinder finite-element model similar to that used by Scheer and Nairn (1995). The model was divided into nine-node isoparametric rectangular elements (100 elements in the axial direction and 45 elements in the transverse direction). The transverse length of the model was determined as $\sqrt{2/3}(d_{\max}/2)$ using the procedure described in Scheer and Nairn (1995). Here, the maximum droplet diameter $d_{\max}$ can be obtained as a function of the embedded fiber length l based on the results shown in Fig. 5. In the model, fiber is represented as an elastic orthotropic material, while the matrix is represented by a J_2 flow elastic–plastic material. The simulation used the material properties listed in Table 1.

To simulate the debonding process during the fiber pullout, interfacial fracture was addressed in the model by incorporating six-node interface elements embedding the damage process zone at the fiber–matrix interface. These elements are based on the EPZ model that relates the separation and traction between solid elements. The damage process in the EPZ model is addressed by the traction-separation constitutive rule and the energy-based criterion. We recently presented a simple EPZ model (Okabe et al., 2006; Nishikawa et al., 2007a) based on Dugdale's assumption (Dugdale, 1960), as illustrated in Fig. 10, and applied this EPZ model to the modeling for the fracture of the fiber–matrix interface (Nishikawa et al., 2007b; Nishikawa et al., in press). Here, we will briefly describe this EPZ model. The constitutive law acts as a penalty function, maintaining the continuity of the displacement between solid elements while the embedded process zone is intact. After the traction reaches its maximum value $T_{i,\max}$ ($i = \mathrm{I}, \mathrm{II}$), where subscript i denotes the separation mode of the element, the traction remains constant until complete separation occurs at a critical value Δ_{ic} ($i = \mathrm{I}, \mathrm{II}$). The critical separation and maximum traction are related to the critical energy release rate G_{ic} ($i = \mathrm{I}, \mathrm{II}$) as

$$\Delta_{ic} = \frac{G_{ic}}{T_{i,\max}} + \frac{T_{i,\max}}{2k_1} \tag{3}$$

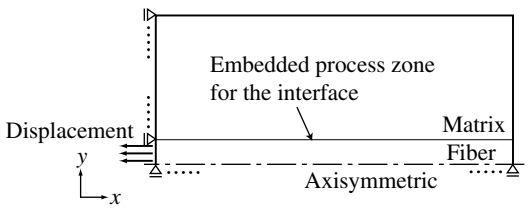

Fig. 9. Schematic diagram of the two-cylinder model.

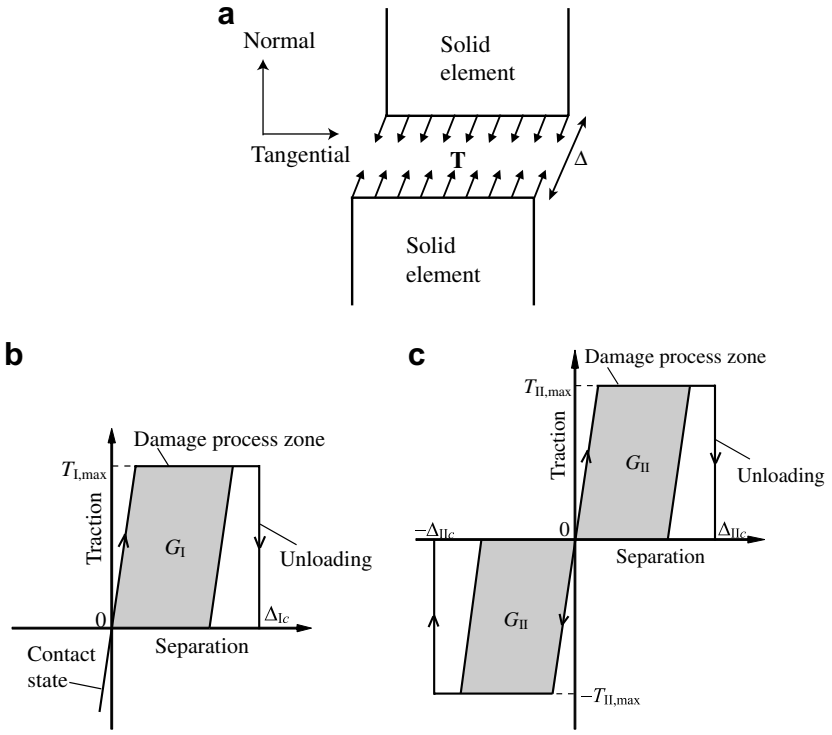

Fig. 10. EPZ model representing the interfacial fracture. (a) Schematic of the element embedding the damage process zone. (b) Normal direction. (c) Tangential direction.

where k_1 denotes the tangent modulus when the embedded process zone is intact. When the damage process is in progress under mixed-mode conditions, it is simply assumed that the traction-separation rule is independently defined in each mode of the elements, irrespective of the separation state in the other mode. In this case, the complete separation condition is defined as

$$D \equiv \left(\frac{\langle \Delta_I \rangle}{\Delta_{Ic}}\right)^2 + \left(\frac{\Delta_{II}}{\Delta_{IIc}}\right)^2 = 1 \tag{4}$$

$$\text{where} \quad \langle \Delta_I \rangle = \begin{cases} \Delta_I & \Delta_I \geqslant 0 \\ 0 & \Delta_I < 0 \end{cases}$$

When Eq. (4) is satisfied at an integration point of an element, all components of the traction at the corresponding point are set to zero. The detailed formulation of these elements into finite-element analysis was discussed in our previous papers (Okabe et al., 2006; Nishikawa et al., 2007a,b). In this approach, interfacial fracture is controlled by a two-parameter set: the maximum traction $T_{II,max}$ and the critical energy release rate G_{IIc}. Here, the present study assumes $T_{I,max} = T_{II,max}$ and $G_{Ic} = G_{IIc}$ regarding mode-I components for simplicity.

With this model, the debonding process during fiber pullout was simulated by controlling the fiber-end displacement. The other boundary conditions are indicated in Fig. 9. The associated fiber-end forces were calculated by summing up the nodal forces at the boundary. The pullout force can then be determined as the maximum fiber-end force during the simulated fiber pullout process.

3.2. Results and discussions

As described above, we attempted to evaluate the interfacial properties based on the upper limit of the experimental results by simulating debonding growth. Fig. 11 compares the simulated results with the exper-

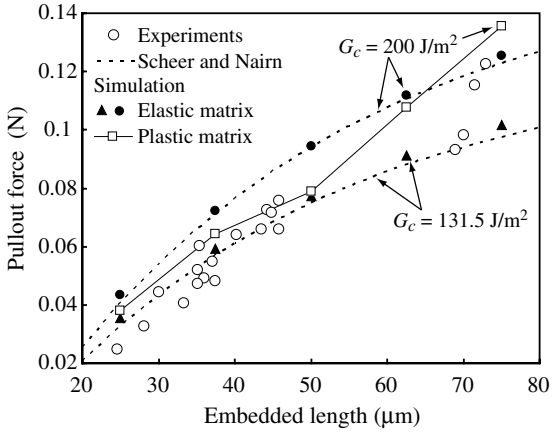

Fig. 11. Comparison of the pullout force between experiments and simulation.

iments. We will focus on the square-plot results (obtained using an elastic–plastic material as matrix) seen in Fig. 11. The simulated results with a particular set of interfacial parameters ($T_{\mathrm{II,max}} = 150$ MPa, $G_{\mathrm{IIc}} = 200$ J/m^2) reasonably represent the upper limit of the experimental results. (The set of the interfacial parameters was obtained through a trial and error process. Here, the uniqueness of the obtained parameters remains an issue. This kind of matter was discussed in Bi et al., 2002; Nishikawa et al., in press). The obtained critical energy release rate (200 J/m^2) needed to fit the upper limit of the experiments implies that the average value (131.5 J/m^2) calculated from the experimental results as presented in Section 2.1 was much underestimated. This is a consequence of our assumption that the upper limit of the pullout force is controlled by the pure debonding process.

For comparison, Fig. 11 also includes simulated results assuming an elastic matrix in place of the elastic–plastic matrix. These results were calculated using the same elastic material properties listed in Table 1. Since the analytical model is based on a variational mechanics model (Scheer and Nairn, 1995) that inherently assumes an elastic matrix, the simulated results for an elastic matrix yield the same tendency of the pullout force as a function of the fiber embedded length as given by the analytical model (Fig. 11). However, the results with the elastic–matrix simulation and the analytical model are significantly different from the simulation for elastic–plastic matrix.

In addition, though the IFSS criterion appears to work better than an energy-based analysis assuming elastic matrix in Fig. 2, Fig. 2 does not truly validate the IFSS criterion due to the overly simplified assumption of constant interfacial stress. The energy-based analysis considering matrix plasticity is essential to represent the upper limit of experimental results over the whole range of the fiber embedded length.

From these results, we can conclude that matrix plasticity is a key factor in quantifying the relevant interfacial properties. Moreover, the present approach, which evaluates the upper limit of the experiments while considering matrix plasticity, will provide a solution to the problem in which the parameters describing interfacial fracture obtained through microbond tests tend to be underestimated in comparison with other single-fiber methods, as reported by Herrera-Franco and Drzal (1992).

4. Influence of the matrix cracking position and cracking force on the fiber pullout

In the preceding section, we assumed that the upper limit of the pullout force for a constant initial embedded length is controlled by a pure debonding process. Finally, this assumption is verified by investigating the influence of matrix cracking on the pullout force. For this purpose, we conducted numerical simulations for the debonding process during fiber pullout with EPZ model, while introducing the matrix cracking in the droplet at a pre-determined cracking force. In particular, we examined the influence of matrix cracking position to clarify the difference of the reduction in pullout force caused by matrix cracking. In addition,

we examined the cases where the matrix cracking force was varied, since the matrix cracking force is an uncertain factor in experiments.

4.1. Numerical model

Here, we again used the finite-element model in Fig. 4. We present the results in this section when the embedded length of the fiber in the model was set to 52 μm. Fiber was represented as an elastic orthotropic material, consisting of nine-node isoparametric quadrilateral elements, and the matrix was represented by a J_2 flow elastic–plastic material, consisting of six-node triangle elements. We used the material properties listed in Table 1. The simulation was conducted by controlling the fiber-end displacement. In addition, the knife-edge position was set to 11.5 mm away from the fiber–matrix interface. This boundary condition was addressed by fixing the corresponding nodes of the droplet boundary whenever they reached the knife-edge as a consequence of deformation.

To estimate the influence of matrix cracking on the pullout force, two types of matrix cracking ((A) large cracking in the droplet and (B) cracking in the meniscus region) were assumed based on the experimental results in Fig. 3. The positions of these cracks are depicted in Fig. 12(a). To examine the effect of the cracking force on the pullout process, each type of crack was introduced at various pre-determined cracking forces. Fig. 12(b) schematically illustrates the introduction of matrix cracking into the finite-element model. The stiffness and stress of matrix elements in the pre-determined crack path were eliminated from the model when the fiber-end force reached a certain pre-determined cracking force during the simulation.

The interfacial fracture was then addressed in the model by incorporating six-node elements embedding the damage process zone at the fiber–matrix interface, as described in Section 3.1. Based on this finite-element model, we simulated the debonding process during fiber pullout, while considering the influence of matrix cracking.

4.2. Results and discussions

The simulated pullout force (i.e. the maximum fiber-end force during the pullout) varies with the crack position and cracking force. Typical simulated results for one set of interface parameter ($T_{\mathrm{II,max}} = 100$ MPa

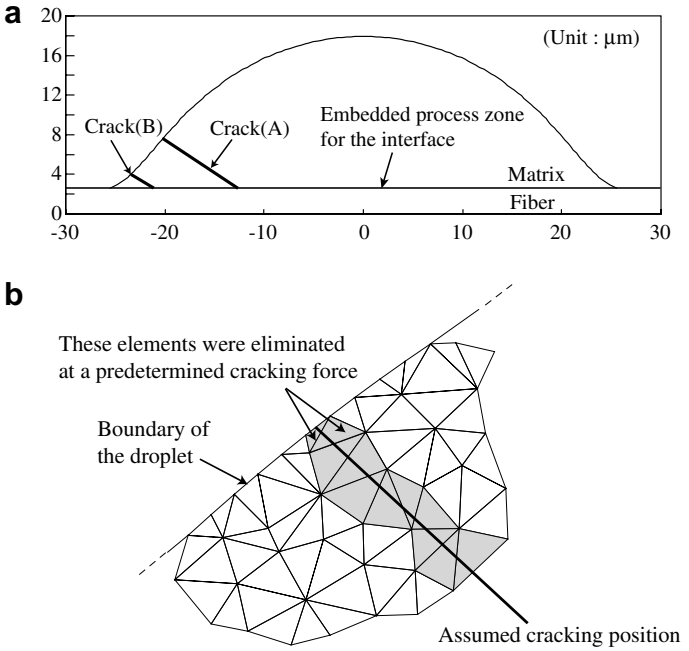

Fig. 12. Schematic diagram of the model used in the pullout simulation with consideration to the influence of matrix cracking. (a) Schematic of the model. (b) Schematic of the method to introduce matrix cracking.

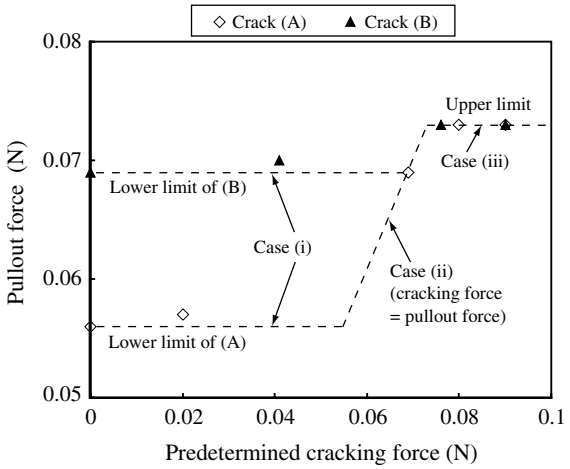

Fig. 13. Simulated pullout force as the crack position and cracking force varies.

and $G_{IIc} = 200$ J/m^2) are summarized in Fig. 13. The simulated pullout force converges to a constant value as the pre-determined cracking force increases. The simulated results are roughly divided into three cases (cases (i) to (iii) as indicated in Fig. 13). When the cracking force is small (case (i)), the fiber-end force increases even after matrix cracking until interfacial debonding occurs. When the cracking force is intermediate (case (ii)), the maximum force is controlled by the cracking force. When the cracking force is large (case (iii)), interfacial debonding occurs before the fiber-end force reaches the cracking force. In case (i), the pullout force is reduced, since the residual length of the fiber embedded in the droplet decreases due to the matrix cracking. Cases (i) and (iii) yield the lower and upper limits of the pullout force, when the embedded length is constant and the position of matrix cracking in the droplet is fixed. In addition, let us now focus on the comparison between cases (A) and (B) in Fig. 13. The influence of matrix cracking (A) on the pullout force causes a reduction of up to 23 %, considering that the upper limit of the pullout force results from the pure debonding process. In contrast, the influence of cracking in the meniscus region is almost negligible as shown by the comparison between the cases (i) and (iii).

Therefore, variation of the matrix cracking size, depending on the knife-edge position as seen in Section 2, inherently causes a variation in pullout force. From the results above, however, we can further conclude that the upper limit of the pullout force for a constant embedded length is controlled by the pure debonding process. Even if the cracking force is less than the force at the propagation of the debonding, the pullout force after the cracking in the meniscus region is almost the same as that of the pure debonding process. This case actually exists, according to the knife-edge position, as discussed in Section 2. For these reasons, we can evaluate the upper limit of the experimental data all over the range of the embedded fiber length, using the simulation without considering matrix cracking, as demonstrated in Section 3. Therefore, the analysis assuming a pure debonding process and repeated experiments obtaining the upper limit of multiple data points contribute to the appropriate evaluation of interfacial fracture, since the upper limit of the pullout force is controlled almost entirely by a pure debonding process.

5. Conclusions

The present study has focused on a micromechanical understanding of the microbond test with consideration given to matrix failure in order to quantify the interface properties of fiber-reinforced composites.

The experimental results and FE modeling reinforces our understanding that the inherent difficulty in controlling the knife-edge position causes the variation of matrix cracking, and consequently the data scatter in the microbond tests. When the knife-edge is near the fiber, the crack from the knife-edge position reaches the fiber–matrix interface. When the knife-edge is far from the fiber, the crack appears in the meniscus region of the droplet. In addition, cracking in the meniscus region hardly influences the maximum force at fiber-pullout,

while matrix cracking from the knife-edge is large enough to cause a significant reduction of the pullout force. These results indicate that the latter failure is a primary cause of the large scatter in the pullout force in experiments. In our simulation, if the knife-edge position is kept more than approximately twice the fiber diameter away from the interface, the fiber can be pulled out without causing a significant matrix cracking. This is an ideal condition of microbond tests in order to evaluate the appropriate interface properties.

Considering the realistic situation, it is rather desirable to extract the interfacial properties from microbond tests while excluding the influence of matrix failure, instead of controlling the knife-edge position precisely. We then discuss how to best extract the interfacial properties while excluding the influence of matrix plasticity and cracking, using numerical simulations. The key mechanisms demonstrated here are that the pullout force converges to a constant value as the cracking force increases, and that the pullout force after the matrix cracking in the meniscus region is almost the same as that of the pure debonding process. The pullout force in these cases appears as the upper limit of the pullout force in the experiment with a constant embedded length of the fiber. Based on this discussion, we can conclude that this upper-limit force is controlled almost entirely by the pure debonding process. This is the principal reason why simple averaging data-reduction underestimates the critical energy release rate for the interfacial fracture. In fact, the upper-limit force all over the range of embedded fiber length in experiments can be reasonably evaluated with the simulation focusing solely on the debonding process with matrix plasticity. This evaluation technique is effective for the appropriate evaluation of the interfacial properties, while excluding the influence of matrix plasticity and cracking on the microbond test results.

Acknowledgements

We acknowledge the support of the Ministry of Education, Culture, Sports, Science and Technology of Japan under Grants-in-Aid for Scientific Research (No. 18760515, No. 17-11722). We are very grateful to Prof. S. Ogihara (Tokyo University of Science) for his cooperation and for many helpful discussions.

Appendix A. Determination of the profile of a matrix droplet on a cylindrical fiber

Here, we describe the procedure to determine the profile of a matrix droplet as a function of the contact angle of the droplet with the fiber, using Carroll's theory (Carroll, 1976). Fig. 6 includes the coordinate system of the fiber–droplet system. We assume that the effect of gravity on the droplet is negligible for this small-diameter fiber and droplet. The profile of the droplet (i.e. the curve of the droplet boundary) can then be expressed for a cylindrical fiber with the auxiliary variable φ, which denotes the angle between a point of the droplet boundary and the y-axis, as follows:

$$y^2 = h^2(1 - k^2 \sin^2 \varphi) \tag{A.1}$$

$$x = \pm(ar_f F(\varphi, k) + hE(\varphi, k)) \tag{A.2}$$

$$\text{where} \quad a = \frac{h\cos\theta - r_f}{h - r_f \cos\theta} \tag{A.3}$$

$$k^2 = \frac{h^2 - a^2 r_f^2}{h^2} \tag{A.4}$$

where θ is the contact angle of the droplet on the fiber as illustrated in Fig. 6, r_f denotes the fiber radius, h denotes the maximum droplet radius given by $h = d_{max}/2$, and F and E are the Legendre's standard incomplete integrals of the first and second kind as a function of auxiliary variable φ and parameter k. Now let us consider the contact points of the droplet on the fiber. Since the coordinates of these points are $(x, y) = (\pm l/2, r_f)$, the following equations are derived from Eqs. (A.1) and (A.2):

$$r_f^2 = h^2(1 - k^2 \sin^2 \varphi_{max}) \tag{A.5}$$

$$l = 2(ar_f F(\varphi_{max}, k) + hE(\varphi_{max}, k)) \tag{A.6}$$

These two equations determine the unknown parameters ($\varphi_{\max}$ and θ), since the embedded length of the fiber l and maximum droplet radius h can be obtained from the experimental data. Then the profile of the droplet is determined through Eqs. (A.1) and (A.2).

Appendix B. One-parameter damage mechanics model for matrix cracking

Here, we describe the method for addressing the matrix cracking in the droplet with the present finite-element simulation. It is difficult to apply the energy-based approach to matrix cracking for the following reasons:

(1) The initiation of matrix cracking needs to be addressed, and the initial position of a crack cannot be determined before the simulation.
(2) A numerical procedure for determining the crack direction is complicated.

Therefore, we have recently developed a one-parameter damage mechanics model for the cracking in epoxy-matrix (Nishikawa et al., in preparation). We applied this model to simulate the microscopic damage in single-fiber composite tests using carbon-fiber and epoxy-matrix system, and demonstrated that the proposed model can reasonably reproduce the characteristic transverse matrix cracking from a fiber break in the tests. Then the present simulation utilizes this continuum damage mechanics model to deal with the matrix cracking during microbond tests. We will explain this model below.

Our model utilizes the formulation of one-parameter damage mechanics model given by Kobayashi et al. (2004), which simplifies the Murakami–Ohno model (Murakami and Ohno, 1981) and defines the damage variable as scalar quantity. We begin with defining strain-equivalent configuration. The variables in the nominal state (macroscopically homogenized state, or the state used in finite-element calculation) (stress σ, strain ε, stiffness E) can be expressed in relation to those in the true state (actual, microscopically damaged state) (σ^*, ε^*, E_0) as follows. (Here, we write down one-dimensional description for simplicity.)

$$\varepsilon^* = \varepsilon, \quad E = (1-D)E_0 \;\rightarrow\; \sigma^* = \frac{\sigma}{1-D} \tag{B.1}$$

where D denotes the damage variable causing the stiffness degradation. As D increases, the stiffness reduces till finally $E = 0$ when $D = 1$. For the elastic–plastic matrix, the multi-dimensional incremental stress–strain relations can be derived as below.

$$\Delta\boldsymbol{\sigma} = (1-D)\mathbf{C}^{\mathrm{ep}} : \Delta\boldsymbol{\varepsilon} - \frac{\Delta D}{1-D}\boldsymbol{\sigma} \tag{B.2}$$

where $\boldsymbol{\varepsilon}$ and $\boldsymbol{\sigma}$ denotes the strain and stress tensors, and $\mathbf{C}^{\mathrm{ep}}$ is the elastic–plastic constitutive tensor. Here, the damage variable D is defined as scalar quantity.

The microscopic failure characteristics in the matrix material can be incorporated into the evolutionary equation of damage variable. Here, we define the following evolutionary equation of damage variable.

$$\begin{aligned} &\Delta D = (1-D)C\langle\Delta\varepsilon_{\mathrm{m}}^{\mathrm{p}}\rangle + (B_0 + B_1 D)\Delta\bar{\varepsilon}^{\mathrm{p}} \qquad (0 \leqslant D \leqslant 1) \\ &\text{where} \quad C\Delta\varepsilon_{\mathrm{m}}^{\mathrm{p}} = A\Delta\{D(\langle\sigma_{\mathrm{m}}\rangle/\sigma_{\mathrm{y}})^2\} \end{aligned} \tag{B.3}$$

The first term represents the extension of existing voids or defects due to plastic volumetric expansion strain $\varepsilon_{\mathrm{m}}^{\mathrm{p}}$ (referring to the famous equation by Gurson, 1977), while the second term represents the damage extension due to shear failure. $\bar{\varepsilon}^{\mathrm{p}}$ denotes the plastic equivalent strain, σ_{m} is the mean stress, and σ_{y} is the matrix yield stress. The meaning of the bracket $\langle\ \ \rangle$ in Eq. (B.3) is similar to that in Eq. (4) and Eq. (B.3). As D increases, the contribution of the first term reduces, which means that the void growth is suppressed by neighboring voids, and then the shear failure dominates. This reflects the microscopic situations in epoxy fracture. The phenomelogical parameters A, B_0, and B_1 in Eq. (B.3) are reasonably calibrated through the comparison with SFC test results (Nishikawa et al., in press). Then, we use the calibrated parameters $A = 0.5$, $B_0 = 0$, $B_1 = 0.5$, and $D_{\mathrm{ini}} = 0.01$ as the initial value of D.

Matrix cracking is judged at the integration point of each finite element. When D approaches 1, the contribution to the stiffness matrix becomes near zero and sometimes numerical instability occurs. Therefore, we eliminated the corresponding element when the averaged D in the element reaches D_{cr} (near 1). The present simulation uses $D_{cr} = 0.9$. The successive elimination process yields free nodes, which are not referred to by the intact elements. Such nodes are searched for and excluded from the equilibrium equations of the finite-element analysis. By this procedure, we can simulate the initiation and propagation of matrix cracking.

References

Ash, J.T., Cross, W.M., Svalstad, D., Kellar, J.J., Kjerengtroen, L., 2003. Finite element evaluation of the microbond test: meniscus effect, interphase region, and vise angle. Composites Science and Technology 63, 641–651.

Bi, X., Li, Z., Guebelle, P.H., Lambros, J., 2002. Dynamic fibre debonding and frictional push-out in model composite systems: numerical simulations. Mechanics of Materials 34, 433–466.

Carroll, B.J., 1976. The accurate measurement of contact angle, phase contact areas, drop volume, and Laplace excess pressure in drop-on-fiber systems. Journal of Colloid and Interface Science 57, 488–495.

Dugdale, D.S., 1960. Yielding of steel sheets containing slits. Journal of the Mechanics and Physics of Solids 8, 100–104.

Gurson, A.L., 1977. Continuum theory of ductile rupture by void nucleation and growth: Part I – Yield criteria and flow rules for porous ductile media. Transactions of the ASME – Journal of Engineering Materials and Technology, 2–15.

Herrera-Franco, P.J., Drzal, L.T., 1992. Comparison of methods for the measurement of fibre/matrix adhesion in composites. Composites 23, 2–27.

Hutchinson, J.W., Evans, A.G., 2000. Mechanics of materials: top down approaches to fracture. Acta Materialia 48, 125–135.

Kobayashi, S., Tomii, D., Shizawa, K., 2004. A modelling and simulation on failure prediction of ductile polymer based on craze evolution and annihilation. Transactions of the Japan Society of Mechanical Engineers A 70, 810–817 (in Japanese).

Miller, B., Muri, P., Rebenfeld, L., 1987. A microbond method for determination of the shear strength of a fibre/resin interface. Composites Science and Technology 28, 17–32.

Murakami, S., Ohno, N., 1981. A continuum theory of creep and creep damage. Creep in Structures. Springer-Verlag, pp. 422–444.

Nishikawa, M., Okabe, T., Takeda, N., 2007a. Numerical simulation of interlaminar damage propagation in CFRP cross-ply laminates under transverse loading. International Journal of Solids and Structures 44, 3101–3113.

Nishikawa, M., Okabe, T., Takeda, N., 2007b. Finite element analysis for microscopic damage in single-fiber composites using a cohesive zone model. Journal of the Japan Society for Composite Materials 33, 170–177 (in Japanese).

Nishikawa, M., Okabe, T., Takeda, N., in press. Determination of interface properties from experiments on the fragmentation process in single-fiber composites. Materials Science and Engineering, doi:10.1016/j.msea.2007.07.067.

Nishikawa, M., Okabe, T., Shokinji T., Takeda, N., Curtin, W. A., in preparation. Microstructure-dependent fracture mode of short-fiber reinforced plastic composites.

Nutt, S.R., Needleman, A., 1987. Void nucleation at fiber ends in Al–SiC composites. Scripta Metallurgica 21, 705–710.

Okabe, T., Nishikawa, M., Takeda, N., 2006. Numerical simulation of tensile damage evolution in FRP cross-ply laminates. Transactions of the Japan Society of Mechanical Engineers A 72, 1254–1261 (in Japanese).

Scheer, R.J., Nairn, J.A., 1995. A comparison of several fracture mechanics methods for measuring interfacial toughness with microbond tests. Journal of Adhesion 53, 45–68.

Tsai, J.H., Patra, A., Wetherhold, R., 2005. Finite element simulation of shaped ductile fiber pullout using a mixed cohesive zone/friction interface model. Composites A 36, 827–838.

Tvergaard, V., 1990. Effect of fiber debonding in a whisker-reinforced metal. Materials Science and Engineering A 125, 203–213.

Zhao, F.M., Takeda, N., Inagaki, K., Ikuta, N., 1996. A study on interfacial shear strength of GF/epoxy composites by means of microbond tests. Advanced Composite Letters 5, 113–116.

Zinck, P., Wagner, H.D., Salmon, L., Gerard, J.F., 2001. Are microcomposites realistic model of the fibre/matrix interface? Polymer 42, 5401–5413.